

Detection and Location of Gamma-Ray Sources With a Modulating Coded Mask

Dale N. ANDERSON, David C. STROMSWOLD,
Sharon C. WUNSCH, Anthony J. PEURUNG,
and Randy R. HANSEN

Pacific Northwest National Laboratory
Richland, WA 99352
(dale.anderson@pnl.gov)

The detection of high-energy γ -ray sources is vitally important to national security for numerous reasons, particularly nuclear materials smuggling interdiction and threat detection. This article presents two methods of detecting and locating a concealed nuclear γ -ray source by analyzing detector data of emissions that have been modulated with a coded mask. The advantages of each method, derived from a simulation study and experimental data, are discussed. Energetic γ -rays readily penetrate moderate amounts of shielding material and can be detected at distances of many meters. Coded masks are spatial configurations of shielding material (e.g., small squares formed from plates of lead or tungsten) placed in front of a detector array to modulate the radiation distribution. A coded mask system provides improved detection through an increased signal-to-noise ratio. In a search scenario it is impossible to obtain a comparison background run without the presence of a potential concealed source. The developed analysis methods simultaneously estimate background and source emissions and thus provide the capability to detect and locate a concealed high-energy radiological source in near real time. An accurate source location estimate is critically important to expedite the investigation of a high-probability γ -ray source. The experimental examples presented use a proof-of-concept coded mask system of a 4×4 array of NaI detectors directed at a γ -ray source in a field-of-view roughly 4 m wide \times 3 m high (approximately the size of the side panel of a small freight truck). Test results demonstrate that the correct location of a radiologic source could be determined in as little as 100 seconds when the source was 6 m from the detector.

KEY WORDS: Gamma-ray detection; Homeland security; Poisson.

1. INTRODUCTION

Coded masks can be viewed as a suite of single-pinhole cameras arranged mathematically so that the γ -rays emitted from any direction in a field of view produce an almost unique signature on an array of detectors. (See Caroli, Stephen, Di Cocco, Natalucci, and Spizzichino 1987 and Skinner 1984 for a general discussion of coded mask imaging techniques.) Initial applications of coded masks were used in astronomy to image celestial X-ray sources (Skinner 1988). The technology has been used to image radioactive contamination in industrial equipment (Woodring et al. 2003) and for nuclear arms control verification (Schaich, Clark, Sengupta, and Zioc 1996). Zhang and Lanza (1999) used a coded mask to image γ -rays from fast neutron reactions in contraband and explosives. Although imaging technologies are critically important in medical research and practice, coded masks for γ -ray imaging are not used here, because three-dimensional imagery by other techniques (e.g., computer assisted tomography) is substantially superior. For example, Vassilieva and Chaney (2002) noted that after 20 years of research, coded imaging has not been successfully migrated from astronomy to medicine, because medical images behave as distributed sources (near-to-source imaging), and coded mask imaging is optimal when applied to images that behave as point sources. van Eijk (2002) offered a comprehensive review of medical imaging technologies with no mention of coded mask techniques. The astronomy applications image X-rays that are readily stopped by the coded mask material and detected with fine spatial resolution. In contrast, energetic γ -rays, the topic of this article, are more difficult to stop by a coded mask and tend to be diffuse in detection location because of multiple scattering in the detector.

The fundamental contribution of this article is the mathematical demonstration that a coded mask can be used to image high-energy γ -ray sources with a single data-collection run and can provide a simultaneous estimate of background and source. We present experimental results using a constructed mask (Fig. 1) and a 16-detector NaI sensor array to measure γ -rays with energies of approximately 1–3 mega electron volts (MeV). Sources that emit photons in this energy range include cesium-137, cobalt-60, potassium-40, bismuth-214, and thallium-208.

Specific national security applications for which coded masks may be useful include detecting radiation sources transiting international borders, for example, shipping containers (mounted on trailers or rail cars) and trucks used to transport radioactive material used for nuclear weapons components or radiation dispersal devices. Interdicting these sources is often a two-step process. Initially, the presence of elevated radiation is detected through primary screening as vehicles approach a customs or border patrol check station. The primary detectors are nonimaging but are capable of rapid screening of moving vehicles. Detection of high radiation triggers diversion of the vehicle to a secondary screening location, where more detailed examination identifies the cause of the elevated radiation.

A radiation detector with a coded mask could be used in secondary screening, where more time is available to obtain imaging data. A coded mask system would provide the capability of imaging the radiation source's location, compared with

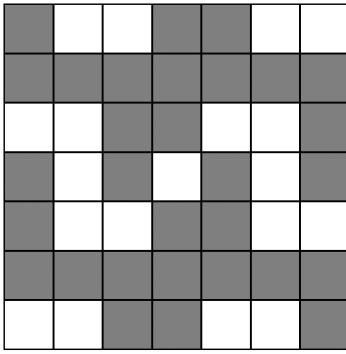


Figure 1. A Graphic of a Coded Mask. The pattern of opaque and transparent squares is designed mathematically, so that any segment of an image of γ -rays will cast an almost unique shadow of radiation on a position-sensitive detector, allowing the direction to the source to be estimated.

conventional searches with hand-held instruments. Conceptually, a coded mask system would survey a vehicle parked for 5–15 minutes (Fig. 2). Measuring background and source simultaneously is important, because any radiation background measured before the vehicle is present will be perturbed by the vehicle and its cargo. In addition, some cargo is weakly radioactive because it contains naturally occurring radioactive materials, such as potassium (e.g., road salt) or thorium (e.g., clay products). Such materials are likely to be evenly distributed in the cargo and constitute a modified background from which a more intense and localized radiation source would need to be distinguished.

As noted by Fenimore (1978) and Fenimore and Cannon (1978), when detecting a point source, a coded mask can increase the signal-to-noise ratio over that of a single-pinhole camera. The degree to which the signal-to-noise ratio is optimized is dependent predominantly on the proportion of the mask that is transparent and the basic pattern of the transparent and opaque squares. A measure of mask effectiveness is the spatial autocorrelation function (SACF). Conceptually, the SACF is computed by laying the basic mask on top of a very large mosaic of itself, moving the basic mask to any position different from perfect registration and calculating the proportion of open area seen through both masks. A perfect, yet impossible mask would have a spike in the SACF with perfect registration and an SACF value of 0 when the registration of two mask patterns is different. Conceptually, a perfect mask would lay completely unique signatures of each field-of-view segment onto a detector array. The region of the SACF when the registration of two mask patterns is different is termed the “side lobes” of the function. If the SACF’s side lobes are constant, then the effects of the coded mask can be effectively removed from the observed detector signatures.

Fenimore and Cannon (1978) have developed the mathematical techniques to construct a mask with an SACF that is always constant when the registration of two mask patterns is different (constant side lobes). These masks are known as uniform redundant arrays (URAs), and their SACF properties effectively optimize the signal-to-noise ratio and construction of an image from observed detector signatures. The mathematical derivation of a URA pattern is based on abstract algebra theory, and particularly cyclic difference set theory. (See Busboom, Elders-Boll,

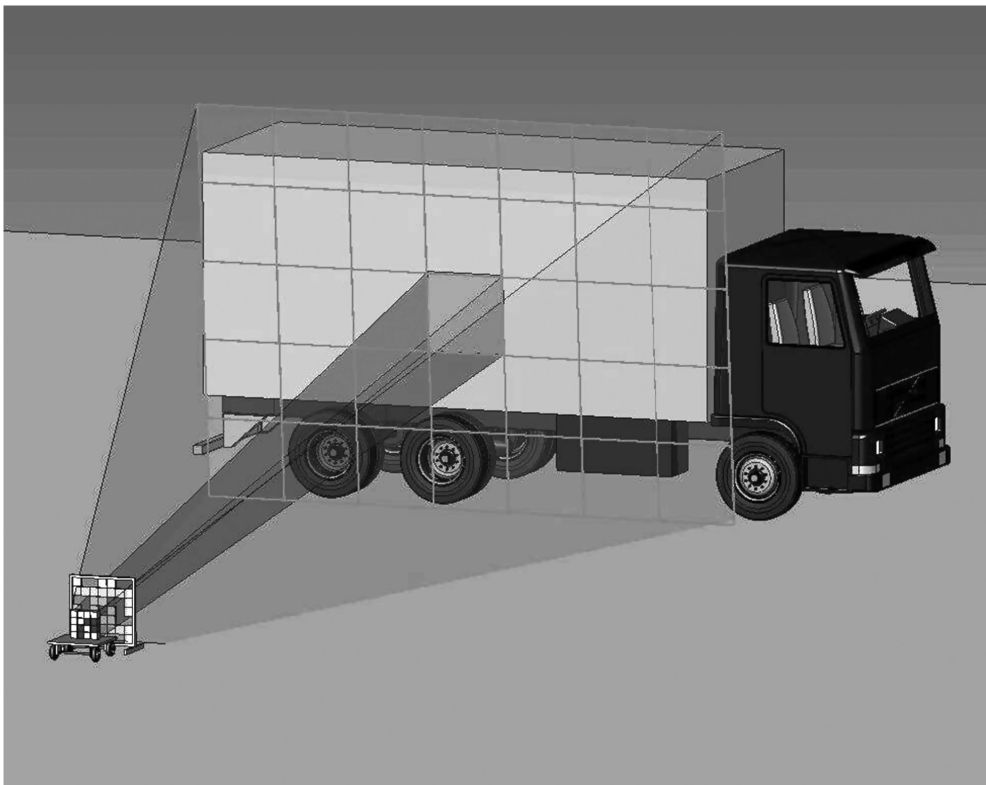


Figure 2. The Operational Use of a γ -Ray Imaging System (coded mask and detector array) to Detect and Locate a Concealed γ -Ray Source. The stacked crates (truck cargo) either emit background or an added localized source (gray crate) of γ -rays.

and Schotten 1998 for a detailed mathematical review of URA construction techniques.) URA patterns are applied to $p \times q$ detector arrays, where p and q are necessarily prime numbers and $p - q = 2$. Gottesman and Fenimore (1989) extended the principles of URA construction for imaging applications to square detector arrays. The construction process for these modified uniform redundant arrays (MURAs) is based on a p (with p a prime number) length sequence of pseudorandom 0's and 1's.

For this project, engineering design considerations and financial constraints prevented the use of a 5×3 URA or a 5×5 MURA. A 4×4 basic mask pattern was needed, and the techniques proposed by Busboom et al. (1997) provided a promising solution. Here a mask pattern is selected from a suite of all possible patterns subject to two constraints. First, the discrete Fourier transform of the mask pattern must not have 0-magnitude components; otherwise, division by 0 will occur in frequency domain image reconstruction (deconvolution). Second, the signal-to-noise ratio is optimized relative to the transmission rate of the mask (the number of transparent elements in the mask pattern). Another highly desirable property of the mask would be a pattern that has constant side lobes in the

SACF. This would ensure that the reconstructed image would be free of systematic bias introduced by the physical mask.

2. CODED MASK IMAGE RECONSTRUCTION

Figure 3 shows a pictorial description of γ -ray propagation through a coded mask onto an array of detectors. The shaded square at the top in each of the 16 graphics represents a localized origin of γ -rays (i.e., background or source location). The γ -rays pass through the coded mask (represented by the middle array of squares) and strike a 4×4 detector array at the bottom (represented by gray squares). The individual graphics in Figure 3 show how γ -rays from various source locations pass through different sections of the coded mask and make it possible to create a unique image on the detectors. The individual pictures are piecewise representations of a simultaneous physical process. Each segment in a field of view emits γ -rays that pass through the coded mask onto the detector array. Note that the shaded mask sections generate an overlapping signature of γ -rays onto the detector array. This physical characteristic of coded mask imaging is mathematically captured as a two-dimensional convolution. For each graphic, one can envision

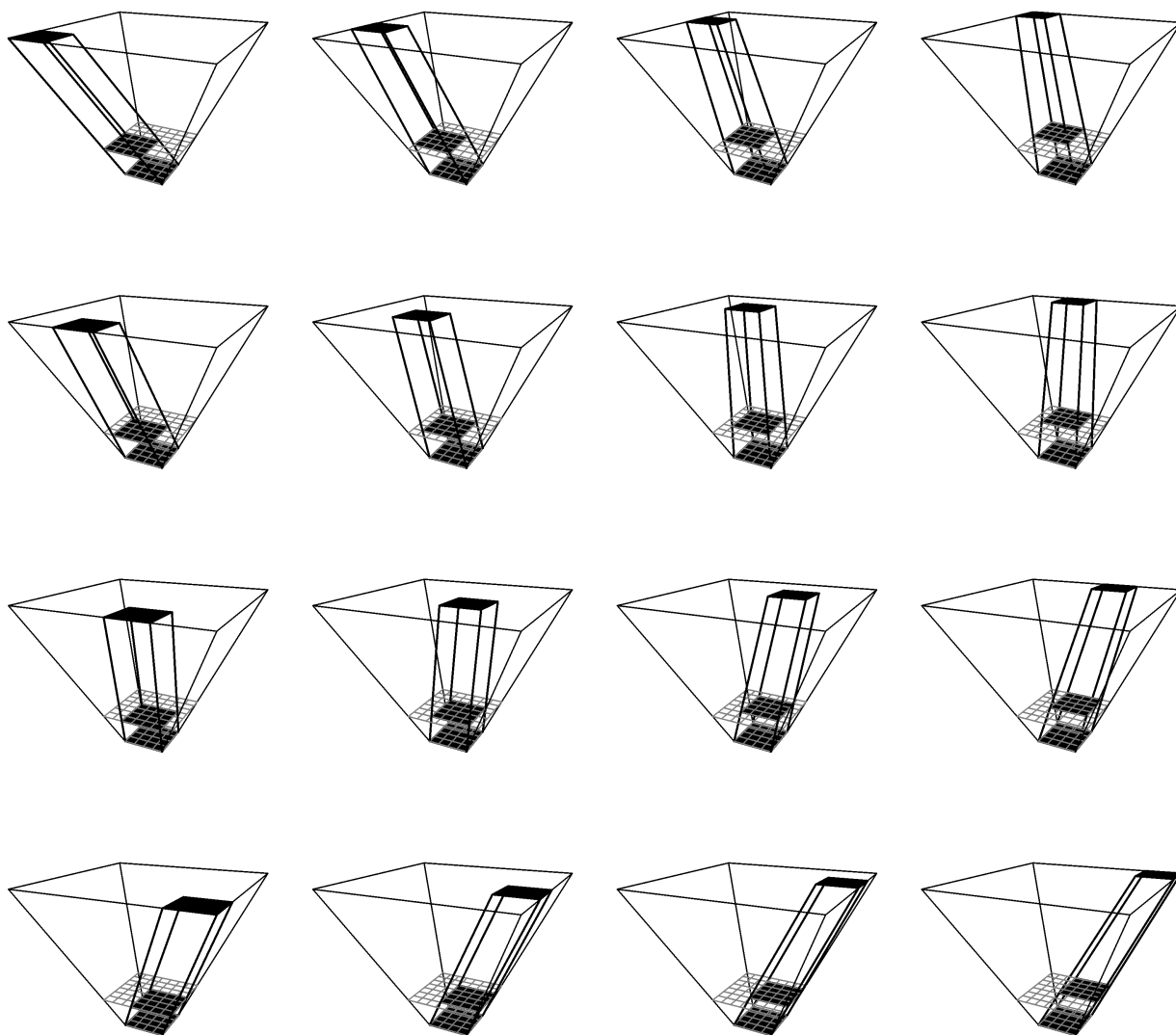


Figure 3. A Pictorial Description of γ -Ray Propagation Through a Coded Mask Onto an Array of Detectors.

the almost unique pattern that would be laid onto the detector if the opaque and transparent squares were represented by the mask array.

This convolution process can be illustrated with a calculation example. Let the photons emitted from a field of view be represented by the 4×4 matrix

$$\mathbf{S} = \begin{pmatrix} n_{11} & n_{12} & n_{13} & n_{14} \\ n_{21} & n_{22} & n_{23} & n_{24} \\ n_{31} & n_{32} & n_{33} & n_{34} \\ n_{41} & n_{42} & n_{43} & n_{44} \end{pmatrix},$$

where n_{ij} is the number of γ -rays from source segment (i, j) incident on the mask (not on the detector). The γ -rays from the field of view are assumed to be uniformly distributed within each of the 16 segments, and the γ -rays can come from a specific source or from background.

The coded mask is mathematically represented by the matrix

$$\mathbf{A} = \begin{pmatrix} 0 & 1 & 1 & 0 & 0 & 1 & 1 \\ 0 & 0 & 0 & 0 & 0 & 0 & 0 \\ 1 & 1 & 0 & 0 & 1 & 1 & 0 \\ 0 & 1 & 0 & 1 & 0 & 1 & 0 \\ 0 & 1 & 1 & 0 & 0 & 1 & 1 \\ 0 & 0 & 0 & 0 & 0 & 0 & 0 \\ 1 & 1 & 0 & 0 & 1 & 1 & 0 \end{pmatrix}. \quad (1)$$

The convolution operator defines the number of photons incident on a detector as a linear combination of the random variables n_{ij} . The statistical analysis of detector data begins with the derivation of the multivariate probability distribution of the detector signatures—a function of the random variables n_{ij} .

Figure 4 is an array of detector counts that correspond to the graphics in Figure 3 after the γ -rays have propagated through the coded mask \mathbf{A} onto the detector. If the detector count matrices in Figure 4 are summed elementwise, then the result is the actual theoretical signature that would be laid onto the detectors

as a result of the coded mask. For example, the theoretical contribution to the $(1, 1)$ detector would be $n_{12} + n_{13} + n_{31} + n_{32} + n_{42} + n_{44}$, and the contribution to the $(1, 2)$ detector would be $n_{11} + n_{12} + n_{31} + n_{34} + n_{41} + n_{43}$.

It is important to note that the matrix representation of the coded mask, \mathbf{A} , is not a design matrix for a generalized linear model. Rather, \mathbf{A} defines the function of the random variables n_{ij} that give the number of photons incident on the detector. With the addition of detector noise \mathbf{E} , the signature \mathbf{D} of the γ -ray flux is mathematically described with the convolution equation

$$\mathbf{D} = \mathbf{S} * \mathbf{A} + \mathbf{E}, \quad (2)$$

where $*$ is the convolution operator. Basic image reconstruction is directly accomplished by neutralizing the convolution effects of the matrix \mathbf{A} . If we replace the zero elements of \mathbf{A} in (1) with g , we get the matrix

$$\mathbf{G} = \begin{pmatrix} g & 1 & 1 & g & g & 1 & 1 \\ g & g & g & g & g & g & g \\ 1 & 1 & g & g & 1 & 1 & g \\ g & 1 & g & 1 & g & 1 & g \\ g & 1 & 1 & g & g & 1 & 1 \\ g & g & g & g & g & g & g \\ 1 & 1 & g & g & 1 & 1 & g \end{pmatrix}, \quad (3)$$

and with an appropriate choice for g , the introduction of \mathbf{G} into (2) will in fact neutralize the convolution of \mathbf{S} with \mathbf{A} . In the special case of $g = -1/2$, we have

$$(\mathbf{S} * \mathbf{A}) * \mathbf{G} = \begin{pmatrix} 6n_{11} & 6n_{12} & 6n_{13} & 6n_{14} \\ 6n_{21} & 6n_{22} & 6n_{23} & 6n_{24} \\ 6n_{31} & 6n_{32} & 6n_{33} & 6n_{34} \\ 6n_{41} & 6n_{42} & 6n_{43} & 6n_{44} \end{pmatrix} = 6\mathbf{S}.$$

From (2),

$$(\mathbf{D} - \mathbf{E}) * \mathbf{G} = (\mathbf{S} * \mathbf{A}) * \mathbf{G} = \mathbf{S}_0, \quad (4)$$

$$\begin{pmatrix} 0 & n_{11} & n_{11} & 0 \\ 0 & 0 & 0 & 0 \\ n_{11} & n_{11} & 0 & 0 \\ 0 & n_{11} & 0 & n_{11} \end{pmatrix} \begin{pmatrix} n_{12} & n_{12} & 0 & 0 \\ 0 & 0 & 0 & 0 \\ n_{12} & 0 & 0 & n_{12} \\ n_{12} & 0 & n_{12} & 0 \end{pmatrix} \begin{pmatrix} n_{13} & 0 & 0 & n_{13} \\ 0 & 0 & 0 & 0 \\ 0 & 0 & n_{13} & n_{13} \\ 0 & n_{13} & 0 & n_{13} \end{pmatrix} \begin{pmatrix} 0 & 0 & n_{14} & n_{14} \\ 0 & 0 & 0 & 0 \\ 0 & n_{14} & n_{14} & 0 \\ n_{14} & 0 & n_{14} & 0 \end{pmatrix} \\ \begin{pmatrix} 0 & 0 & 0 & 0 \\ n_{21} & n_{21} & 0 & 0 \\ 0 & n_{21} & 0 & n_{21} \\ 0 & n_{21} & n_{21} & 0 \end{pmatrix} \begin{pmatrix} 0 & 0 & 0 & 0 \\ n_{22} & 0 & 0 & 0 \\ n_{22} & 0 & n_{22} & n_{22} \\ n_{22} & n_{22} & 0 & 0 \end{pmatrix} \begin{pmatrix} 0 & 0 & 0 & 0 \\ 0 & 0 & n_{23} & n_{23} \\ 0 & n_{23} & 0 & n_{23} \\ n_{23} & 0 & 0 & n_{23} \end{pmatrix} \begin{pmatrix} 0 & 0 & 0 & 0 \\ 0 & n_{24} & n_{24} & 0 \\ n_{24} & 0 & n_{24} & 0 \\ 0 & 0 & n_{24} & n_{24} \end{pmatrix} \\ \begin{pmatrix} n_{31} & n_{31} & 0 & 0 \\ 0 & n_{31} & 0 & n_{31} \\ 0 & n_{31} & n_{31} & 0 \\ 0 & 0 & 0 & 0 \end{pmatrix} \begin{pmatrix} n_{32} & 0 & 0 & n_{32} \\ n_{32} & 0 & n_{32} & 0 \\ n_{32} & n_{32} & 0 & 0 \\ 0 & 0 & 0 & 0 \end{pmatrix} \begin{pmatrix} 0 & 0 & n_{33} & n_{33} \\ 0 & n_{33} & 0 & n_{33} \\ n_{33} & 0 & 0 & n_{33} \\ 0 & 0 & 0 & 0 \end{pmatrix} \begin{pmatrix} 0 & n_{34} & n_{34} & 0 \\ n_{34} & 0 & n_{34} & 0 \\ 0 & 0 & n_{34} & n_{34} \\ 0 & 0 & 0 & 0 \end{pmatrix} \\ \begin{pmatrix} 0 & n_{41} & 0 & n_{41} \\ 0 & n_{41} & n_{41} & 0 \\ 0 & 0 & 0 & 0 \\ n_{41} & n_{41} & 0 & 0 \end{pmatrix} \begin{pmatrix} n_{42} & 0 & n_{42} & 0 \\ n_{42} & n_{42} & 0 & 0 \\ 0 & 0 & 0 & 0 \\ n_{42} & 0 & 0 & n_{42} \end{pmatrix} \begin{pmatrix} 0 & n_{43} & 0 & n_{43} \\ n_{43} & 0 & 0 & n_{43} \\ 0 & 0 & 0 & 0 \\ 0 & 0 & n_{43} & n_{43} \end{pmatrix} \begin{pmatrix} n_{44} & 0 & n_{44} & 0 \\ 0 & 0 & n_{44} & n_{44} \\ 0 & 0 & 0 & 0 \\ 0 & n_{44} & n_{44} & 0 \end{pmatrix}$$

Figure 4. A Suite of Detector Count Matrices Resulting From the Propagation of γ -Rays Through a Coded Mask [eq. (1)] Onto an Array of Detectors. The actual observed counts for each detector are the elementwise sum of each matrix in this suite.

where \mathbf{S}_0 emulates the original field of view \mathbf{S} . Several values of g can be used, each with a different physical interpretation. We have used a value of $g = -3/5$ for the analysis presented in Section 5. Technical interpretation for this and two other values of g is given in Section 4.2.

Equation (2) can be written as a matrix algebra formulation, facilitating the derivation of the multivariate distribution of \mathbf{D} and \mathbf{S}_0 . The details of how to construct these matrices are deferred to the Appendix. With the matrix \mathbf{S} vectorized, $\vec{\mathbf{S}}' = (n_{11}, n_{12}, \dots, n_{43}, n_{44})$, (2) can be written with the $\vec{\mathbf{A}}$ matrix formulation

$$\vec{\mathbf{D}} = \vec{\mathbf{A}}\vec{\mathbf{S}} + \vec{\mathbf{E}}. \quad (5)$$

Here $\vec{\mathbf{D}}$ is a 16×1 vector of convolved counts on each detector [see (A.2)], and $\vec{\mathbf{E}}$ is a 16×1 vector of detector noise. $\vec{\mathbf{A}}$ is the linear algebra representation of the coded mask matrix \mathbf{A} and is developed in the Appendix. The matrix version of the reconstruction equation is then

$$\vec{\mathbf{G}}(\vec{\mathbf{D}} - \vec{\mathbf{E}}) = \vec{\mathbf{G}}(\vec{\mathbf{A}}\vec{\mathbf{S}}) = \vec{\mathbf{S}}_0, \quad (6)$$

where $\vec{\mathbf{G}}$ is the matrix version of the deconvolution matrix \mathbf{G} and developed in the Appendix. Equation (5) also suggests that image reconstruction can be accomplished directly by inverting the matrix $\vec{\mathbf{A}}$. In some applications this is entirely feasible; however, as a general rule, coded mask design matrices ($\vec{\mathbf{A}}$) with binary elements are often ill-conditioned (Caroli et al. 1987). Image reconstruction and analysis is usually accomplished with the application of $\vec{\mathbf{G}}$ and $\vec{\mathbf{S}}_0$.

3. MASK DEVELOPMENT

We applied the techniques proposed by Busboom et al. (1997) to develop a 4×4 coded mask pattern. In our application of these techniques, we observed that with eight open squares (transmission rate of 50%) in the basic 4×4 mask patterns, the side lobes of the SACF were variable, with a maximum value of 6. Thus, with this mask transmission rate, some pairs of object segments will pass through the mask and propagate a near-equal signature onto the detector array. This will erode, if not destroy, the ability to estimate the location of a source in the field of view. With seven open squares in the basic mask, the side lobes are variable in the operational mask with a maximum value of 3, and with five open squares the side lobes are variable with a maximum value of 2. However, a 4×4 basic mask pattern with a transmission rate of 37.5% (six open

squares) has constant SACF side lobes with a value of 2. We selected a basic 4×4 mask with this transmission rate.

For this configuration, there are a total of 192 masks, 4 of which are shown in Figure 5. Any of the 192 masks could be used in operations. The mask pattern used in this article, presented in Figure 1, is a mosaic of the basic 4×4 mask with one row and column removed. Removing a row and column from the basic mask ensures that the segments in the field of view lay almost unique signatures onto the detector array (see Caroli et al. 1987). The transmission rate for the operational 7×7 mask is approximately 40% (19/49). Referring again to Figure 4, when any two matrices are overlapped, they always have exactly two non-0 elements, giving the value 2 for the side lobes. This is precisely the property indicated by the SACF for this mask pattern. Application of this mask in detecting and locating a γ -ray source is discussed in Sections 4 and 5.

4. SOURCE DETECTION AND LOCATION

Our development is specific to the mask matrix \mathbf{A} in (1) but can be directly generalized to other masks. The n_{ij} 's are independent Poisson random variables with expected value $\mu_{ij}t$. Here t is in seconds, and μ_{ij} has dimension γ -rays/second. We consider the scenario where only one pixel in the field of view contains a source. This scenario is consistent with the anticipated operational setting. Without loss of generality, we let n_{11} be Poisson with mean and variance λt (source plus background), and let all other n_{ij} 's be Poisson with mean and variance μt (background only).

Two approaches to source detection and location are developed. One is based on image reconstruction with deconvolution—a classical hypothesis test approach. The other is based on image reconstruction with (4). A simulation study is summarized demonstrating the performance differences between the two methods. The noise term \mathbf{E} in (2) is negligible for this application; however, for some high-energy sources, the material used for opaque segments of a coded mask is unable to stop all γ -rays (leakage). This effect and various count times are folded into the simulation as parameters.

4.1 A Multiple-Hypothesis Test Procedure for Source Detection and Location

If the matrix $\vec{\mathbf{A}}$ is nonsingular (see Sec. 2), then $\vec{\mathbf{S}}_1 = \vec{\mathbf{A}}^{-1}\vec{\mathbf{D}}$ is an image reconstruction through deconvolution. Further, the elements of $\vec{\mathbf{S}}_1$ are approximate independent Poisson

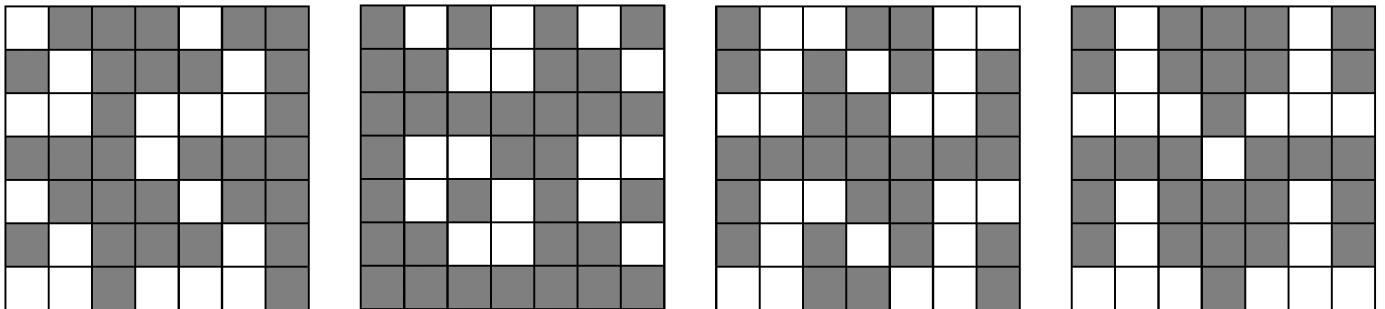


Figure 5. A Sample of the 192 Mosaicked 4×4 Masks With the Last Row and Column Deleted (operational masks). Removing a row and column from the mosaicked mask ensures that the segments in the field of view lay almost unique signatures onto the detector array.

random variables. With a sufficiently long count time t , the transformed variables $\bar{\mathbf{Y}} = \sqrt{\mathbf{S}_1}$ are approximately independent Gaussian, and the delta method can be used to demonstrate that the variables $\bar{\mathbf{Y}}$ all have variance $1/4$. With $\ell = (1 \ -1/15 \ -1/15 \ \dots \ -1/15 \ -1/15)$, and under the null hypothesis that the emissions in image segment $(1, 1)$ are less than or equal to the average emissions of all other segments, the linear combination $\ell\bar{\mathbf{Y}}$ is approximately Gaussian with mean 0 and variance $\ell\ell'/4$. Large values of $\ell\bar{\mathbf{Y}}$ relative to the variance $\ell\ell'/4$ reject the null hypothesis. Each of the 16 image segments can be tested for significance above the average of all others with this theory by cycling the 1 in ℓ through all 16 vector positions. Rejecting any of the 16 hypothesis tests is both a detection and a source location.

Because 16 single tests will be calculated on the same count run, the single-test type I error rate (α') must be adjusted to give the necessary overall error (α) of detecting a source when there is only background in the field of view. We apply a Bonferroni adjustment to α . For example, if operations will permit $\alpha = 10$ in 5,000 unnecessary inspections at a port of entry into a country, then the single-test error rate, α' , should be about $\frac{10}{5,000} \frac{1}{16} \approx .0001$.

4.2 An Ad Hoc Procedure for Source Detection and Location

We also propose an ad hoc procedure constructed loosely from statistical concepts. We present this approach because in experimental studies it has proven quite accurate, and it is based on established approaches to coded mask analysis designed to avoid the calculation of \mathbf{A}^{-1} . There are exactly six elements of $\theta_{\mathbf{D}}$ that equal $(5\mu + \lambda)t$ and ten elements that equal $6\mu t$. The position of these elements changes depending on the position of the field-of-view pixel with the source; however, there are always six $(5\mu + \lambda)t$ and ten $6\mu t$ elements in $\theta_{\mathbf{D}}$. With a sufficient count time, the Poisson model [eq. (A.1) in the App.] becomes Gaussian. Equation (A.3) in the Appendix describes the mean and covariance of the modulated γ -rays entering the detectors. Equation (6) gives the reconstructed image with mean $\theta_{\tilde{\mathbf{S}}_0}$ and covariance $\Sigma_{\tilde{\mathbf{S}}_0}$.

For large t , we can approximate the Poisson model (A.1) with the multivariate Gaussian distribution. A value in the reconstructed image is a point source if it is larger than a background critical value. For example, for $g = -1/2$, a value in the reconstructed image \mathbf{S}_0 is a point source if it is larger than a background critical value $6\mu t + z_{\alpha'}\sqrt{6\mu t}$. Here $z_{\alpha'}$ is an appropriate standard Gaussian critical value. This background critical

value is simply constructed from the theoretical mean and variance of a background random variable in \mathbf{S}_0 . The critical values for other values of g and computational interpretation are listed in Table 1.

As in Section 4.1, we apply a Bonferroni adjustment to α . If operations will permit $\alpha = 10$ in 5,000 unnecessary inspections at a port of entry into a country, then the single-test error rate α' should be about $\frac{10}{5,000} \frac{1}{16} \approx .0001$, which gives a value of $z_{\alpha'} \approx 3.7$.

In application, we need an estimate of the background parameter μ . If a source is present, then it is assumed to be in one and only one field-of-view segment (as described in Sec. 4). The remaining 15 pixels produce background γ -rays. Propagating this field of view through the mask, ten of the detectors will measure only background counts and six will include signal counts as summarized with (A.2) and (A.3). Intuitively, this suggests that for large t , the ten smallest detector counts from a counting experiment could be combined to form an estimate of background, and the signal could be estimated using the six largest detector counts. Denote the observed detector counts by c_{ij} and the ordered counts by $c_{(i)}$. To estimate μ and λ , we equate the sum of the first q order statistics ($T_{\text{Min}} = \sum_{i=1}^q c_{(i)}$) to $q6\mu t$ and the sum of the largest p ($T_{\text{Max}} = \sum_{i=16-p+1}^{16} c_{(i)}$) order statistics to $p(5\tilde{\mu} + \tilde{\lambda})t$. These equations give parameter estimates by solving for $\tilde{\mu}$ and $\tilde{\lambda}$. Specifically, the parameter estimate equations are

$$\tilde{\mu} = \frac{T_{\text{Min}}}{6qt} \quad \text{and} \quad \tilde{\lambda} = \frac{T_{\text{Max}}}{pt} - 5\tilde{\mu}. \quad (7)$$

These estimates of background and source can then be substituted into the appropriate pixel significance equation (Table 1) to determine whether a reconstructed image pixel (Sec. 2) is significantly above background.

4.3 Simulated Performance

This section summarizes the analysis of simulated detector data with the approaches described in Sections 4.1 and 4.2. A field of view was simulated with the Poisson model described in Section 4. Detector data were then generated with the error term (\mathbf{E}) equal to 0. A leakage effect was simulated by replacing the zero elements in (1) with the value .4. The leakage factor in the simulation emulates the fact that for some high-energy sources, the modulating effect of a coded mask can be diminished. Count times (t) were 100, 200, and 500 seconds, and each simulation was replicated 10,000 times. To properly compare the power of the two approaches, the performance of

Table 1. Image Reconstruction Parameter Values and Associated Pixel Significance Critical Values Specific to the Coded Mask Equation (1)

g	Computational effect	Critical value
-1/2	Pixel intensities in the reconstructed image are 6 times the number of γ -ray counts incident on mask elements.	$6(\mu t + z_{\alpha'}\sqrt{\mu t})$
-7/12	The sum of intensities in the reconstructed image equals the total γ -ray counts incident on mask.	$\frac{1}{3}(-\lambda t + 4\mu t + z_{\alpha'}\sqrt{(\lambda + 338\mu)t})$
-3/5	The sum of intensities in the reconstructed image is 0.	$\frac{2}{5}(-\lambda t + \mu t + z_{\alpha'}\sqrt{(\lambda + 239\mu)t})$

Table 2. A Summary of the Simulated Performance of the Multiple Hypothesis and Ad Hoc Analysis of Coded Mask Detector Data

	<i>t</i>	Hypothesis	Ad hoc
No leakage	100	.94	.94
	200	.94	.95
	500	.93	.96
Leakage	100	.94	~1
	200	.94	~1
	500	.94	~1

NOTE: The field of view is background (emission rate of $\mu t = .15t$ in all field-of-view segments). The table elements are the proportion of correct decisions out of 10,000. All table entries are rounded to the nearest hundredth.

each was calibrated to be equal for background emissions, no leakage, and $t = 100$. The tables that follow summarize the simulations.

The ad hoc procedure generally has slightly better false-alarm performance than the multiple-hypothesis test procedure. The two methods have similar detection performance with no leakage. The hypothesis test is clearly superior with leakage, and it is interesting to note that with lower source intensities, the ad hoc procedure has better location performance after detection. With moderate leakage, the multiple-hypothesis test procedure should be used unless longer count times are implemented. Coded mask design matrices ($\hat{\mathbf{A}}$) with binary elements are often ill-conditioned (see Sec. 2) and in this situation, with increased count time t , the ad hoc procedure provides a technically sound approach for detection and location.

Table 3. A Summary of the Simulated Performance of the Multiple Hypothesis and Ad Hoc Analysis of Coded Mask Detector Data

λ		<i>t</i>	Hypothesis	Ad hoc
.19	No leakage	100	.09 (.50)	.10 (.49)
		200	.13 (.67)	.12 (.70)
		500	.30 (.89)	.26 (.90)
	Leakage	100	.08 (.48)	~0 (.93)
		200	.12 (.68)	~0 (~1)
		500	.30 (.89)	.03 (~1)
.23	No leakage	100	.21 (.84)	.23 (.83)
		200	.44 (.94)	.43 (.95)
		500	.88 (.99)	.86 (.99)
	Leakage	100	.21 (.86)	.01 (.98)
		200	.45 (.95)	.06 (~1)
		500	.89 (.99)	.47 (~1)
.26	No leakage	100	.46 (.95)	.49 (.95)
		200	.81 (.99)	.80 (.99)
		500	~1 (~1)	~1 (~1)
	Leakage	100	.46 (.95)	.09 (~1)
		200	.81 (.99)	.34 (~1)
		500	~1 (~1)	.94 (~1)
.30	No leakage	100	.72 (.98)	.73 (.98)
		200	.97 (~1)	.96 (~1)
		500	~1 (~1)	~1 (~1)
	Leakage	100	.71 (.98)	.26 (~1)
		200	.96 (~1)	.71 (~1)
		500	~1 (~1)	~1 (~1)

NOTE: The field of view has a source in the (1, 4) position [emission rate of $\mu t = .15t$ in 15 field-of-view segments and $\lambda t = .19t, .23t, .26t, .30t$ in the (1, 4) segment]. The table elements are the proportion of correct decisions out of 10,000, with the proportion of correct source position estimates reported in parentheses. All table entries are rounded to the nearest hundredth.

5. EXPERIMENTAL EXAMPLES

The detector contains a 4×4 array of 16 NaI detectors, each of which is $7.6 \times 7.6 \times 10.2$ cm. The square sides of the detector permit a high density of NaI by positioning multiple detectors side by side, and the size of each detector is suitable for stopping energetic (1–3 MeV) γ -rays. The detectors are partially shielded from background radiation by placing them inside a 6.3-cm-thick copper box with only one open side. Signals from the detectors are processed separately, resulting in 16 γ -ray spectra. The coded mask is constructed of tungsten squares ($7.6 \times 7.6 \times 1.27$ cm) arranged in the pattern specified in Figure 1 and the matrix \mathbf{A} in (1). Tungsten that is 1.27 cm thick will not fully attenuate 1–3 MeV γ -rays; emissions are reduced by a factor of 30–40% rather than the theoretical value of 0 in (1). Photographs of the operational proof-of-concept system, NaI detector array and coded mask are given in Figure 6.

The distance from the detectors to the coded mask can be adjusted in accordance with the size of the target image area. To image a large area, the mask is located close to the detectors, and to image a smaller area with increased resolution, the mask can be moved away from the detectors. For this application, the data were collected with the coded mask close to the detector (44 cm), giving a field of view of about 3.5×3.5 m at a distance of 6 m from the detector. The coded mask was tested by placing sources at various positions in front of the detector and within its field of view. The distance between the source and detector was 6 m. At this distance, with the coded mask only 44 cm from the detector, near-field effects of imaging are insignificant (Zhang 1998). If the source is too near the detector, then the shadow of the coded mask increases in size before it reaches the detector simply from geometric effects. In our formulation we assume a far-field application setting.

For the ad hoc procedure (Sec. 4.2), a value of $g = -3/5$ (see Table 1) was used. The \mathbf{E} term in (2) is practically negligible. Tables 4–6 give the raw counts in the 16 detectors, the multiple hypothesis test z -scores, and the ad hoc z -scores using order statistics estimates of μ and λ with $q = 10$ and $p = 6$. For fixed source location, maximum likelihood estimates (MLEs) of the parameters μ and λ are developed in the Appendix; these are also presented in Tables 4–6. Experiments of 1,000- and 100-second count times are reported. Table 4 is an analysis of a background-only field of view and serves to illustrate the heterogeneous nature of a typical background. The true position of the source is given in Tables 5 and 6. Any z -score above 3.7 is considered significant. For example, in Table 6 the source was at the (3, 1) position against a wall 6 m in front of the detector, and the ad hoc z -score of 5.14 clearly identifies the (3, 1) position of the source.

In our experience with other experiments, a high-energy γ -ray source at a distance of about 6 m can be accurately located in as little as 100 seconds with the ad hoc procedure, even when source plus background is only 45% greater than background ($\lambda = 1.45\mu$). When the source is not clearly located in one of the distinct 16 segments of the field of view (e.g., it straddles a boundary between segments), longer acquisition times are required. This can be viewed as determining the position of two separated, weaker sources, which takes longer. Tests in which the source was shielded by lead of thickness up to 5 cm



Figure 6. The Operational Proof-of-Concept Coded Mask System. The 4×4 array of NaI detectors, with system electronics and operator interface are housed in the dolly case. Tungsten blocks are attached to a plastic sheet to form the coded mask that is mounted on a frame and positioned in front of the detector array (between the detector array and the field of view).

Table 4. Count Data From the Individual Detectors and z-Scores for the Multiple Hypothesis and Ad Hoc Procedures for a 1,000-Second Count Time

$\begin{pmatrix} 158 & 178 & 170 & 174 \\ 156 & 160 & 147 & 137 \\ 162 & 147 & 151 & 168 \\ 147 & 138 & 137 & 135 \end{pmatrix}$	$\begin{pmatrix} -.83 & .13 & 1.19 & 1.38 \\ -.83 & -.61 & -2.48 & -3.04 \\ 1.51 & 2.17 & 1.24 & 1.10 \\ 1.01 & -.88 & -.23 & -.83 \end{pmatrix}$	$\begin{pmatrix} -.60 & .34 & 1.50 & 1.70 \\ -.60 & -.39 & -2.02 & -2.44 \\ 1.86 & 2.64 & 1.54 & 1.39 \\ 1.28 & -.66 & -.03 & -.60 \end{pmatrix}$
(a) Raw detector counts	(b) z-scores for the multiple hypothesis procedure	(c) z-scores for the ad hoc procedure

NOTE: The field of view is of a typical background.

Table 5. Count Data From the Individual Detectors and z-Scores for the Multiple Hypothesis and Ad Hoc Procedures for a 1,000-Second Count Time

$\begin{pmatrix} 198 & 318 & 312 & 217 \\ 166 & 178 & 201 & 185 \\ 180 & 135 & 265 & 218 \\ 265 & 170 & 244 & 146 \end{pmatrix}$	$\begin{pmatrix} -1.25 & -.89 & -.69 & \mathbf{11.31} \\ -5.49 & -3.06 & -11.54 & -.59 \\ 2.14 & 1.04 & .16 & 1.66 \\ 1.54 & 1.66 & 3.04 & .96 \end{pmatrix}$	$\begin{pmatrix} -.90 & -.57 & -.38 & \mathbf{17.49} \\ -3.96 & -2.41 & -7.41 & -.29 \\ 2.68 & 1.41 & .47 & 2.12 \\ 1.98 & 2.12 & 3.82 & 1.32 \end{pmatrix}$
(a) Raw detector counts	(b) z-scores for the multiple hypothesis procedure	(c) z-scores for the ad hoc procedure

NOTE: The true source position is (1, 4). The ad hoc estimates for the (1, 4) position are $\hat{\mu} = .0296$ and $\hat{\lambda} = .122$, and the MLEs are $\hat{\mu} = .033$ and $\hat{\lambda} = .122$.

Table 6. Count Data From the Individual Detectors and z-Scores for the Multiple Hypothesis and Ad Hoc Procedures for a 100 Second Count Time

$\begin{pmatrix} 25 & 30 & 29 & 18 \\ 15 & 24 & 16 & 26 \\ 26 & 33 & 22 & 18 \\ 16 & 17 & 24 & 20 \end{pmatrix}$	$\begin{pmatrix} 1.62 & 1.10 & -.80 & .76 \\ -1.63 & -1.90 & .39 & -.31 \\ 3.40 & -.46 & -.01 & -.01 \\ 2.08 & 2.08 & 1.58 & 4.58 \end{pmatrix}$	$\begin{pmatrix} 2.12 & 1.39 & -.62 & .96 \\ -1.20 & -1.35 & .53 & -.19 \\ \mathbf{5.14} & -.34 & .096 & .096 \\ -.62 & -.62 & -.91 & .82 \end{pmatrix}$
(a) Raw detector counts	(b) z-scores for the multiple hypothesis procedure	(c) z-scores for the ad hoc procedure

NOTE: The true source position is (3, 1). The ad hoc estimates for the (3, 1) position are $\hat{\mu} = .032$ and $\hat{\lambda} = .123$, and the MLEs are $\hat{\mu} = .003$ and $\hat{\lambda} = .012$.

demonstrated that the correct source location could be determined at even lower signal/background levels when counting times were extended to 3,600 seconds. Additional experiments with the coded mask demonstrated that spectral γ -ray analysis was able to simultaneously locate two separated and isotopically different sources.

6. SUMMARY

Our investigation into coded masks has shown that it is possible to design and construct a near-real time detection system that can determine the location of a radiologic point source emitting γ -rays. Although uniformly redundant arrays are conventional for many coded mask applications and provide optimal performance, they impose design restrictions. Near-optimal performance can be obtained using a combinatorial design for the coded mask that allows the use of square arrays of detectors.

We have demonstrated that the mathematical statistics of coded mask imaging provides estimates of background and source from a single data-acquisition run and, if present, the location of a point source. The ability to locate a point source without independently measuring the background offers a critically significant improvement in the capability to detect and locate radiologic threats. This analysis capability can reduce false-positive indications and expedite investigation of high-probability source locations.

Experimental tests confirmed that a coded mask using a 4×4 array of NaI detectors was able to measure γ -rays and determine the correct source location. When a source was 6 m from the detector, the correct source location was effectively obtained in as little as 100 seconds. At that distance, the counts from the source were only about 45% of background. The coded mask system succeeded in identifying the correct source location, because the source was localized in comparison to the diffuse background coming mainly from the ground.

ACKNOWLEDGMENTS

The authors acknowledge the support of the National Nuclear Security Administration, Office of Nonproliferation Research and Engineering for funding this work. The Pacific Northwest National Laboratory is operated by Battelle for the United States Department of Energy under contract DE-AC06-76RLO 1830. The authors thank the editors and referees for valuable technical suggestions that completed the article and added clarity and rigor.

APPENDIX: MATRIX REPRESENTATION OF CONVOLUTION AND MAXIMUM LIKELIHOOD ESTIMATION

The detector has dimensions 4×4 . The basic mosaicked mask has dimensions 8×8 and the operational mask is 7×7 . Denote the operational mask as $\mathbf{A} = \{a_{ij}\}$, $a_{ij} \in \{0, 1\}$, $i, j = 1, \dots, 7$. Form a new matrix, composed of submatrices \mathbf{W}_{ij} ,

$$\begin{pmatrix} \mathbf{W}_{11} & \mathbf{W}_{12} & \mathbf{W}_{13} & \mathbf{W}_{14} \\ \mathbf{W}_{21} & \mathbf{W}_{22} & \mathbf{W}_{23} & \mathbf{W}_{24} \\ \mathbf{W}_{31} & \mathbf{W}_{32} & \mathbf{W}_{33} & \mathbf{W}_{34} \\ \mathbf{W}_{41} & \mathbf{W}_{42} & \mathbf{W}_{43} & \mathbf{W}_{44} \end{pmatrix},$$

where $\mathbf{W}_{ij} = \{a_{lk}\}$, $l = i, \dots, i + 4 - 1$, $k = j, \dots, j + 4 - 1$. The submatrices \mathbf{W}_{ij} indicate the elements of the source image that contribute to the i, j detector as the source is modulated through the coded mask. The matrix form of \mathbf{A} is then

$$\vec{\mathbf{A}} = \begin{pmatrix} \text{vec}(\mathbf{W}_{11}) \\ \text{vec}(\mathbf{W}_{12}) \\ \vdots \\ \text{vec}(\mathbf{W}_{44}) \end{pmatrix},$$

where $\text{vec}(\mathbf{W}_{ij}) = (\text{row 1 of } \mathbf{W}_{ij}, \text{row 2 of } \mathbf{W}_{ij}, \text{row 3 of } \mathbf{W}_{ij}, \text{row 4 of } \mathbf{W}_{ij})$. The deconvolution matrix $\vec{\mathbf{G}}$ is constructed in the same manner. Note that this formulation is easily generalized to larger and different mask patterns. With $\vec{\mathbf{E}}$ negligible, we have

$\vec{\mathbf{S}} \stackrel{\text{dist}}{=} \text{Poisson}$ with

$$\theta_{\vec{\mathbf{S}}} = \begin{pmatrix} \lambda t \\ \mu t \\ \vdots \\ \mu t \end{pmatrix}, \quad \Sigma_{\vec{\mathbf{S}}} = \begin{pmatrix} \lambda t & 0 & \dots & 0 & 0 \\ 0 & \mu t & \dots & 0 & 0 \\ \vdots & & \ddots & & \vdots \\ 0 & 0 & \dots & 0 & \mu t \end{pmatrix}. \quad (\text{A.1})$$

Here $\theta_{\vec{\mathbf{S}}}$ is the mean vector for the elements of $\vec{\mathbf{S}}$ and $\Sigma_{\vec{\mathbf{S}}}$ is the covariance matrix. Fundamental multivariate calculations (see, e.g., Press 1982) give

$$\vec{\mathbf{D}} = \begin{pmatrix} n_{12} + n_{13} + n_{31} + n_{32} + n_{42} + n_{44} \\ n_{11} + n_{12} + n_{31} + n_{34} + n_{41} + n_{43} \\ \vdots \\ n_{12} + n_{14} + n_{21} + n_{24} + n_{43} + n_{44} \\ n_{11} + n_{13} + n_{23} + n_{24} + n_{42} + n_{43} \end{pmatrix} = \vec{\mathbf{A}} \vec{\mathbf{S}} \quad (\text{A.2})$$

with

$$\theta_{\vec{\mathbf{D}}} = \vec{\mathbf{A}} \theta_{\vec{\mathbf{S}}} \quad \text{and} \quad \Sigma_{\vec{\mathbf{D}}} = \vec{\mathbf{A}} \Sigma_{\vec{\mathbf{S}}} \vec{\mathbf{A}}'. \quad (\text{A.3})$$

For fixed source location, the probability model that describes the propagation of the field of view through the mask is defined by (A.1), (A.2), and (A.3). Varying the source parameter λt across all field-of-view segments (i, j) defines 16 probability

models (likelihoods) for observed $\vec{\mathbf{D}}$. The background-only model is defined by placing the parameter μt in all of the field-of-view segments. All of these likelihoods are defined by (A.1), (A.2), and (A.3). For fixed t , the maximum likelihood estimates, $\hat{\mu}$ and $\hat{\lambda}$ for the 16 source-present models and $\hat{\mu}$ alone for the background-only model, are the values that maximize each of these likelihood functions. For a single source in the field of view, the marginal asymptotic distribution of the maximum likelihood estimates of μ and λ is derived by Lehmann (1983). From direct application of this theory, we have

$$\begin{pmatrix} \hat{\lambda} \\ \hat{\mu} \end{pmatrix} \xrightarrow{d} \text{MVN} \left[\begin{pmatrix} \lambda \\ \mu \end{pmatrix}, \begin{pmatrix} \frac{2\lambda^2}{1+2t\lambda} & 0 \\ 0 & \frac{\mu^2}{15(1+\mu t)} \end{pmatrix} \right]. \quad (\text{A.4})$$

[Received June 2002. Revised March 2005.]

REFERENCES

- Busboom, A., Elders-Boll, H., and Schotten, H. D. (1997), "Combinatorial Design of Near-Optimum Masks for Coded Aperture Imaging," in *Proceedings of the IEEE International Conference Acoustics, Speech, and Signal Processing*, Piscataway, NJ: IEEE Press, pp. 2817–2820.
- (1998), "Uniformly Redundant Arrays," *Experimental Astronomy*, 8, 97–123.
- Caroli, E., Stephen, J. B., Di Cocco, G., Natalucci, L., and Spizzichino, A. (1987), "Coded Aperture Imaging in X and Gamma Ray Astronomy," *Space Science Reviews*, 45, 349–403.
- Fenimore, E. E. (1978), "Coded Aperture Imaging: Predicted Performance of Uniformly Redundant Arrays," *Applied Optics*, 17, 3562–3570.
- Fenimore, E. E., and Cannon, T. M. (1978), "Coded Aperture Imaging With Uniformly Redundant Arrays," *Applied Optics*, 17, 337–347.
- Gottesman, S. R., and Fenimore, E. E. (1989), "New Family of Binary Arrays for Coded Aperture Imaging," *Applied Optics*, 28, 4344–4352.
- Lehmann, E. L. (1983), *Theory of Point Estimation*, New York: Wiley.
- Press, S. J. (1982), *Applied Multivariate Analysis: Using Bayesian and Frequentist Methods of Inference*, Malabar, FL: Krieger.
- Schaich, P. C., Clark, G. A., Sengupta, S. K., and Ziocck, K.-P. (1996), "Automatic Image Analysis for Detecting and Quantifying Gamma-Ray Sources in Coded Aperture Images," *IEEE Transactions on Nuclear Science*, 43, 2419–2426.
- Skinner, G. K. (1984), "Imaging With Coded Aperture Masks," *Nuclear Instruments and Methods in Physics Research*, 221, 33–40.
- (1988), "X-Ray Imaging With Coded Masks," *Scientific American*, August, 84–89.
- van Eijk, C. W. E. (2002), "Inorganic Scintillators in Medical Imaging," *Physics in Medicine and Biology*, 47, R85–R106.
- Vassilieva, O. I., and Chaney, R. C. (2002), "Method for Reducing Background Artifacts From Images in Single-Photon Emission Computed Tomography With a Uniformly Redundant Array Coded Aperture," *Applied Optics*, 41, 1454–1461.
- Woodring, M., Beddingfield, D., Souza, D., Entine, G., Squillante, M., Christian, J., and Kogan, A. (2003), "Advanced Multi-Dimensional Imaging of Gamma-Ray Radiation," *Nuclear Instruments & Methods in Physics Research A*, 505, 415–419.
- Zhang, L. (1998), "Near-Field Three-Dimensional Coded Aperture Techniques: Theoretical and Experimental Exploration for Applications in Imaging and Detector Systems," unpublished doctoral thesis, Massachusetts Institute of Technology.
- Zhang, L., and Lanza, R. C. (1999), "Coded Aperture Fast Neutron Analysis for Contraband Detection: Preliminary Results," *IEEE Nuclear Science Symposium Conference Record*, 3, 353–355.